(Received 23 December 2023, Accepted 27 January 2024, Scheduled 13 February 2024)

Decoupling Control of Bearingless Permanent Magnet Synchronous Motor Based on Least Squares Support Vector Machine Inverse System Optimized by Improved Grey Wolf Optimization Algorithm

Huangqiu Zhu[1], Jiankun Du[1], and Gai Liu[2,*]

[1] School of Electrical and Information Engineering, Jiangsu University, Zhenjiang 212013, China
[2] School of Electrical and Control Engineering, Xuzhou University of Technology, Xuzhou 221018, China

ABSTRACT: The characteristics of nonlinear and strong coupling of a bearingless permanent magnet synchronous motor (BPMSM) greatly affect the improvement of its control performance. In the traditional decoupling control of least squares support vector machine (LSSVM) inverse system, the kernel function parameter σ and regularization parameter c are determined according to the empirical value, but not the nonoptimal value, so large error exists in the decoupling control. Therefore, this paper proposes a decoupling control method of LSSVM inverse system based on improved grey wolf optimization algorithm (IGWO). Firstly, the working principle of the BPMSM is described, and the mathematical model is derived. Secondly, the reversibility of the BPMSM is analyzed, and the σ and c of LSSVM are optimized by IGWO, before establishing a generalized inverse system for decoupling control. Thirdly, the simulation tests of the speed regulation and anti-interference are carried out, which show that the decoupling performance of the proposed method is better than the traditional LSSVM inverse system method. Finally, the dynamic experiments, static experiments, and anti-interference experiments are carried out. The feasibility and superiority of the proposed method are verified according to the built experimental platform.

1. INTRODUCTION

The traditional permanent magnet synchronous motor uses mechanical bearings to support the rotor. When the motor runs at high speed, there is a large friction force between the mechanical bearing and the rotor, which will lead to bearing wear and noise, resulting in reducing the service life of the motor and reducing the system efficiency. In order to solve the above problems, the concept of bearingless motor was firstly proposed in the 1980s [1]. Compared with the traditional motors, a set of suspension windings is embedded in the stator slot of the bearingless motor. By adjusting the current into suspension windings and torque windings, the suspension force and electromagnetic torque can be generated simultaneously, so that rotor of the motor can be suspended, and the motor can rotate.

There are many categories of bearingless motors, among which the bearingless permanent magnet synchronous motor (BPMSM) as a new motor combining magnetic bearing and permanent magnet synchronous motor technology has significant advantages. The BPMSM not only has the characteristics of no mechanical wear, no lubrication, long service life, but also has the characteristics of high power density and high efficiency of permanent magnet synchronous motor, and has a wide application prospect in aerospace, biomedicine, chemical industry, flywheel energy storage, and other fields [2–6]. Therefore, the BPMSM has always been favored by scholars and has become an important research direction of bearingless motor.

The nonlinear and strong coupling of the BPMSM greatly affects its dynamic and static performance, which is not conducive to its application in industrial production. Therefore, the study of high-performance decoupling control has been the focus of the BPMSM. At present, the inverse system method is widely used in the study of decoupling control. By using the inverse system of objects to form a α order integral inverse system realized by available feedback method, the object is compensated into a pseudo-linear system with linear transmission relationship, and the system synthesis is finally completed. In [7] and [8], according to the inverse system theory, the dynamic decoupling control algorithm between the torque and radial suspension force is derived to linearize and decouple the nonlinear system into three independent linear subsystems. But the calculation process of finding the inverse system by analytical method is too complicated, too dependent on the mathematical model, and there are large errors. Refs. [9, 10] combine the decoupling linearization characteristics of inverse system with the nonlinear approximation ability of neural network, and propose a decoupling control method of neural network, which avoids the huge calculation process of inverse system model and improves the robustness of the system. However, the process of neural network training samples still tends

* Corresponding author: Gai Liu (lg_just@163.com).

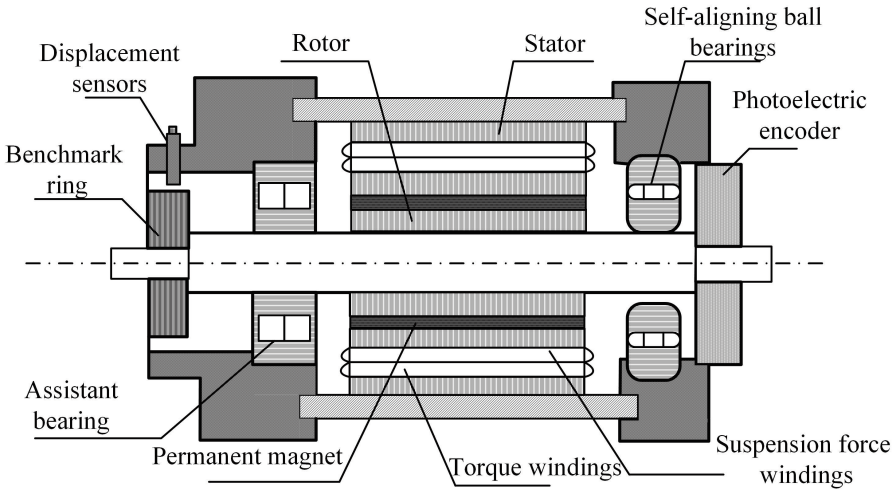

FIGURE 1. Structure diagram of BPMSM.

to fall into the local minimum value and long training time. The decoupling control method of least squares support vector machine (LSSVM) inverse system proposed by [11] fits the inverse system model of the BPMSM through system sample approximation and nonlinear identification, and realizes dynamic decoupling control. Relative to the neural networks, the LSSVM training samples are faster and with higher accuracy.

The kernel function parameter of the LSSVM affects sample complexity of the high-dimensional feature space, and the regularization parameter is responsible for balancing the empirical risk and confidence range of the learning machine. In the traditional method of decoupling control of LSSVM inverse system, the kernel function parameter and regularization parameter are usually determined empirically. Too large error affects the model accuracy, and too small error will lead to overlearning of the system. Therefore, studying the optimal configuration of kernel function parameter and the regularization parameter is crucial.

In [12], genetic algorithm is used to optimize the kernel function parameter and regularization parameter, but there are still some problems such as early maturity, large error in cross rate and variation rate, and difficulty in implementation. Ref. [13] uses the network search method to complete the parameter optimization of the LSSVM, but its calculation amount is huge, and the parameter optimization speed is slow, which is not suitable for the real-time control of the system. Particle swarm optimization (PSO) is used to optimize the parameters of LSSVM in [14]. However, the particle swarm optimization has problems such as falling into local optimality easily and poor robustness.

The grey wolf optimization (GWO) algorithm is a group intelligent optimization algorithm proposed by Mirjalili et al. of Australia in 2014 [15] and is widely used. In [16], the GWO algorithm is used to optimize the back propagation (BP) neural network, and the GWO-BP method provides the best outage probability (OP) performance prediction. Ref. [17] proposes a hybrid approach of hidden Markov model and grey wolf optimization (HMM-GWO) for moisture status (MS) estimation of bushings subjected to the ununiform moisture distribution and dynamic time-series modeling. Ref. [18] combines the GWO and LSSVM for the model establishment of bearingless induction motor, and the GWO-LSSVM modeling has the characteristics of higher accuracy. GWO is well suited for parameter optimization due to its advantages of fewer parameters, rapid optimization process, and easy operation. Therefore, this paper proposes a decoupling control method based on an LSSVM inverse system optimized by improved grey wolf optimization algorithm (IGWO).

The structure of this paper is as follows. In Section 2, the working principle of BPMSM is described, and the mathematical model of radial suspension force and electromagnetic torque is derived, and its reversibility is verified. In Sections 3 and 4, the working principle of the LSSVM optimized based on the IGWO and decoupling model will be described. In Section 5, the simulated effects of the proposed method and the traditional LSSVM inverse system decoupling control are compared and analyzed. The feasibility and superiority of the proposed method are verified through experiment in Section 6. The conclusions of this paper are summarized in Section 7.

2. WORKING PRINCIPLE AND MATHEMATICAL MODEL OF THE BPMSM

2.1. Working Principle of the BPMSM

Literature research shows that the two prerequisites for the suspension operation of the BPMSM are [19]:

(1) The difference between the pole pair number P_{M} of the torque windings and the pole pair number P_{B} of the suspension force windings is 1.

(2) The magnetic field rotation direction and electrical angular velocity of the suspension windings are the same as the magnetic field of the torque windings.

In this paper, the study object is two-degrees of freedom BPMSM. The structure of the BPMSM is show in Fig. 1. The two-degree of freedom BPMSM is mainly composed of torque windings, suspension force windings, photoelectric encoder,

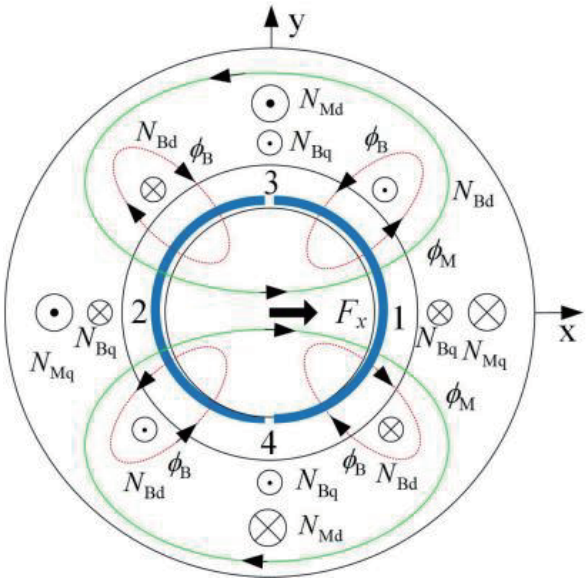

FIGURE 2. Schematic diagram of the radial suspension force generation.

and self-aligning ball bearing. The two sets of windings realize the rotation and suspension functions of the rotor, respectively. The photoelectric encoder detects the speed of the motor, and the self-aligning ball bearing realizes the radial and axial positioning of the other end of the rotor.

The pole pair number of the torque windings and the suspension force windings are 1 and 2, respectively. The principle of radial suspension force generation of the BPMSM is shown in Fig. 2.

As shown in Fig. 2, there are 4-pole suspension windings N_{Bd} and N_{Bq}, and 2-pole torque windings N_{Md} and N_{Mq} are in the stator groove. When both the N_{Bd} and N_{Bq} access currents are zero, the 2-pole magnetic flux Φ_{M} is evenly distributed, and no suspension force is generated. When N_{Bd} enters the positive current, the 4-pole magnetic flux Φ_{B} is generated, and the equilibrium magnetic field Φ_{M} is broken, resulting in the increase of the magnetic density of the air gap on the right side of the rotor and the decrease of the two on the left side of the rotor, thus generating the radial suspension force F_{x} in the positive direction of the x axis; if the N_{Bd} is negative, the radial suspension force in the negative direction of the x-axis will be generated. Similarly, the radial suspension force F_{y} along the y axis can be obtained when the corresponding current is applied into the windings N_{Bq} channel. Therefore, by controlling the current passing into the suspension force windings N_{Bd} and N_{Bq}, the size and direction of the suspension force can be controlled, thus realizing the stable suspension of the BPMSM.

2.2. Mathematical Model of the BPMSM

The mathematical model is established by Maxwell tensor method. When the eccentric displacement in the x- and y-axes is x and y, respectively, the mathematical model of radial suspension force in the coordinates of d-q axis is as follows:

$$\begin{bmatrix} F_x \\ F_y \end{bmatrix} = (k_M + k_L) \begin{bmatrix} \psi_{Md} & \psi_{Mq} \\ \psi_{Mq} & -\psi_{Md} \end{bmatrix} \cdot \begin{bmatrix} i_{Bd} \\ i_{Bq} \end{bmatrix} + k_C \begin{bmatrix} x \\ y \end{bmatrix} \quad (1)$$

where i_{Bd} and i_{Bq} are the components of the suspension force windings current on the d-q axis; ψ_{Md} and ψ_{Mq} are the components of the torque gap magnetic chain on the d-q axis; k_{M} is the Maxwell force constant; k_{L} is the Lorentz force constant; and k_{C} is the constant coefficient.

Considering the mutual interaction and eccentric displacement of windings and rotor, the mathematical model of electromagnetic torque of the BPMSM is established as:

$$\begin{aligned} T_e &= P_M L_M i_f i_{Mq} + x P_B L_C i_f i_{Bd} + y P_B L_C i_f i_{Bq} \\ &\quad + \begin{bmatrix} i_{Md} & i_{Mq} \end{bmatrix} \cdot \begin{bmatrix} L_C x & -L_C y \\ L_C y & L_C x \end{bmatrix} \cdot \begin{bmatrix} -i_{Bd} \\ i_{Bq} \end{bmatrix} \end{aligned} \quad (2)$$

where P_{M} and P_{B} are the polar pair of the torque windings and the suspension windings, respectively; i_{Md} and i_{Mq} are respectively the components of the torque windings current in the d-q axis; and i_{f} is the equivalent current of the permanent magnet.

L_{M} and L_{C} are:

$$\begin{cases} L_M = \dfrac{\mu_0 \pi l r N_1^2 k_1^2}{4\delta_0} \\ L_C = \dfrac{\mu_0 \pi l r N_1 N_2 k_1 k_2}{8\delta_0^2} \end{cases} \quad (3)$$

where μ_0 is the vacuum permeability; N_1 and N_2 are the number of turns of torque windings and suspension windings, respectively; k_1 and k_2 are the distribution coefficient of torque windings and suspension windings, respectively; l is the length of the motor rotor; r is the radius of the motor rotor; and δ_0 is gas length.

Because the values of the rotor eccentric displacement x and y are very small and negligible in the electromagnetic torque, the mathematical model of the BPMSM can be integrated as:

$$\begin{cases} F_x = (k_M + k_L)(\psi_{Md} i_{Bd} + \psi_{Mq} i_{Bq}) + k_C x \\ F_y = (k_M + k_L)(\psi_{Mq} i_{Bd} - \psi_{Md} i_{Bq}) + k_C y \\ T_e = P_M L_M i_f i_{Mq} \\ \psi_{Md} = L_{Md} i_{Md} + \psi_f \\ \psi_{Mq} = L_{Mq} i_{Mq} \end{cases} \tag{4}$$

where L_{Md} and L_{Mq} are respectively the components of the torque windings inductance on the d-q axis, and Ψ_{f} is the magnetic chain of the BPMSM.

According to the rotor dynamics theory, the rotor dynamic equation of the BPMSM is:

$$\begin{cases} \dfrac{J\dot{\omega}_r}{P_M} = T_e - T \\ m\ddot{x} = F_x - f_x \\ m\ddot{y} = F_y - f_y \end{cases} \tag{5}$$

where m is the mass of the rotor; f_{x} and f_{y} are the interference force applied along x and y, respectively; J is the inertia of the rotor; ω_{r} is the angular velocity of the rotor; and T_{L} is the load torque.

2.3. Reversibility Analysis

(1) The inverse system concept

For a general system with p-dimensional input and q-dimensional output, there is a set of definite initial states $\mathbf{X}(t_0) = \mathbf{X}_0$. The general expression of the system can be expressed as:

$$\begin{cases} \dot{\mathbf{x}} = f(\mathbf{X}, \mathbf{U}) \\ \mathbf{Y} = h(\mathbf{X}, \mathbf{U}) \end{cases} \quad \mathbf{X}(t_0) = \mathbf{X}_0 \tag{6}$$

where $\mathbf{U} = (u_1, u_2, \ldots, u_p)^{\mathrm{T}}$ is the p-dimensional input variable; $\mathbf{X} = (x_1, x_2, \ldots, x_w)^{\mathrm{T}}$ is the w-dimensional state variable; $\mathbf{Y} = (y_1, y_2, \ldots, y_q)^{\mathrm{T}}$ is the q-dimensional input variable.

Let the operator satisfying the input to output mapping relationship be θ, then have:

$$\mathbf{Y} = \boldsymbol{\theta U} \tag{7}$$

If a system Q exists, taking the desired output $\mathbf{Y}$ of the above system as the system Q input and the input $\mathbf{U}$ as the output of the system, calling the system Q the inverse system of the original system.

(2) The reversibility discrimination

To achieve the decoupling control between the angular velocity and radial displacement of the BPMSM, with angular velocity ω_{r} and radial displacement x, y as the output variables of the inverse system. The state variable $\mathbf{X}$, input variable $\mathbf{U}$, and output variable $\mathbf{Y}$ are set as:

$$\begin{cases} \mathbf{X} = (x_1, x_2, x_3, x_4, x_5)^T = (x, y, \dot{x}, \dot{y}, \omega_r)^T \\ \mathbf{U} = (u_1, u_2, u_3, u_4)^T = (i_{Md}, i_{Mq}, i_{Bd}, i_{Bq})^T \\ \mathbf{Y} = (y_1, y_2, y_3)^T = (x, y, \omega_r)^T \end{cases} \tag{8}$$

Replacing Equations (4) and (8) into Equation (5) can obtain the equation of state of the BPMSM as follows:

$$\begin{cases} \dot{x}_1 = x_3 \\ \dot{x}_2 = x_4 \\ \dot{x}_3 = \dfrac{k_M + k_L}{m}(L_{Md} u_1 u_3 + L_{Mq} u_2 u_4 + \psi_f u_3) \\ \qquad + \dfrac{k_C}{m} x_1 - \dfrac{1}{m} f_x \\ \dot{x}_4 = \dfrac{k_M + k_L}{m}(L_{Mq} u_2 u_3 - L_{Md} u_1 u_4 + \psi_f u_4) \\ \qquad + \dfrac{k_C}{m} x_2 - \dfrac{1}{m} f_y \\ \dot{x}_5 = \dfrac{P_M^2 L_M i_f}{J} u_2 - \dfrac{P_M}{J} T_L \end{cases} \tag{9}$$

Guide the output variable $\mathbf{Y}$ until each component contains the input variable $\mathbf{U}$, available:

$$\begin{cases} \ddot{y}_1 = \ddot{x}_1 = \dot{x}_3 = \frac{k_M + k_L}{m}(L_{Md} u_1 u_3 + L_{Mq} u_2 u_4 + \psi_f u_3) \\ \qquad + \frac{k_C}{m} x_1 - \frac{1}{m} f_x \\ \ddot{y}_2 = \ddot{x}_2 = \dot{x}_4 = \frac{k_M + k_L}{m}(L_{Mq} u_2 u_3 - L_{Md} u_1 u_4 + \psi_f u_4) \\ \qquad + \frac{k_C}{m} x_2 - \frac{1}{m} f_y \\ \dot{y}_3 = \dot{x}_5 = \frac{P_M^2 L_M i_f}{J} u_2 - \frac{P_M}{J} T_L \end{cases} \tag{10}$$

The corresponding Jacobi matrix can be obtained:

$$\mathbf{A} = \left[\frac{\partial(\ddot{y}_1, \ddot{y}_2, \dot{y}_3)}{\partial \mathbf{U}}\right] = \frac{k_M + k_L}{m} \cdot \begin{bmatrix} L_{Md} u_3 & L_{Mq} u_4 \\ L_{Md} u_4 & -L_{Mq} u_3 \\ 0 & m P_M^2 L_M i_f / (J k_M + J k_L) \\ L_{Md} u_1 + \psi_f & L_{Mq} u_2 \\ -L_{Mq} u_2 & L_{Md} u_1 + \psi_f \\ 0 & 0 \end{bmatrix} \tag{11}$$

The Jacobi matrix rank $(\mathbf{A}) = 3$, and the relative order of the system is $\alpha = (\alpha_1, \alpha_2, \alpha_3) = (2, 2, 1)$, meets $\alpha_1 + \alpha_2 + \alpha_3 \leq 5$, then the BPMSM is reversible. The right-inverse system function can be expressed as:

$$\begin{cases} \mathbf{u} = \bar{\phi}(\{y_1, \dot{y}_1, y_2, \dot{y}_2, y_3\}, \hat{\mathbf{v}}) \\ \hat{\mathbf{v}} = [\hat{v}_1, \hat{v}_2, \hat{v}_3]^T \end{cases} \tag{12}$$

where $\hat{v}_1 = a_{10} y_1 + a_{11} \dot{y}_1 + a_{12} \ddot{y}_1$, $\hat{v}_2 = a_{20} y_2 + a_{21} \dot{y}_2 + a_{22} \ddot{y}_2$, $\hat{v}_3 = a_{30} y_3 + a_{31} \dot{y}_3$, $\bar{\phi}$ is the equivalent operator.

3. IGWO-LSSVM ALGORITHM

3.1. LSSVM Algorithm

The LSSVM adopts the optimization index of the square term and replaces the equation constraint to transform the quadratic programming problem into the solution of linear equations, which simplifies the computational complexity and is widely applied in function approximation and estimation [20]. LSSVM is used to fit the inverse system model to solve the problems of traditional inverse system model solution method, slow solution speed and dependence on exact mathematical model.

Assuming that given the training sample $\{\mathbf{x}_k, \mathbf{y}_k\}_{k=1}^{l}$, $k = 1, 2, \ldots, l$, x_k, y_k are the input and output, respectively, the nonlinear map $\varphi(x)$ is used to map the sample from the original space to the high-dimensional feature space. Construct the optimal linear regression function in this space:

$$\mathbf{y} = \boldsymbol{\omega}^T \varphi(\mathbf{x}) + \mathbf{b} \tag{13}$$

where ω is the weight vector of the determined feature space, and $\mathbf{b}$ is the threshold value.

Using formula (13) to fit the sample, the optimization problem for the LSSVM is defined as

$$\min \mathbf{J}(\boldsymbol{\omega}, \mathbf{e}) = \frac{1}{2}\boldsymbol{\omega}^T\boldsymbol{\omega} + \frac{1}{2}c\sum_{i=1}^{n}\mathbf{e}_i^2 \tag{14}$$

where $\mathbf{e}$ is the relaxation factor, c the regularization parameters, and n the number of training samples in the training set.

The constraint can be expressed as follows.

$$\mathbf{y}_i = \boldsymbol{\omega}^T\varphi(\mathbf{x}_i) + \mathbf{b} + \mathbf{e}_i, \quad i = 1, \ldots, n \tag{15}$$

The joint Equations (13) and (14) construct the Lagrange functions:

$$\begin{aligned} L(\boldsymbol{\omega}, \mathbf{b}, \mathbf{e}, \alpha) &= \frac{1}{2}\|\boldsymbol{\omega}\|^2 + \frac{1}{2}c\sum_{i=1}^{n}\mathbf{e}_i^2 \\ &\quad - \sum_{i=1}^{n}\alpha_i(\boldsymbol{\omega}^T\varphi(\mathbf{x}_i) + \mathbf{b} + \mathbf{e}_i - \mathbf{y}_i) \end{aligned} \tag{16}$$

where α is a Lagrange multiplier.

To find the minimum value of the Lagrange according to the Carlo-Kuhn-Tker (KKT) optimal condition:

$$\begin{cases} \dfrac{\partial L}{\partial \boldsymbol{\omega}} = \mathbf{0} \to \boldsymbol{\omega} = \displaystyle\sum_{i=1}^{n}\alpha_i\varphi(\mathbf{x}_i) \\ \dfrac{\partial L}{\partial \mathbf{b}} = 0 \to \displaystyle\sum_{i=1}^{n}\alpha_i = 0 \\ \dfrac{\partial L}{\partial \mathbf{e}_i} = 0 \to \mathbf{e}_i = \dfrac{\alpha_i}{\mathbf{c}} \\ \dfrac{\partial L}{\partial \alpha_i} = 0 \to \boldsymbol{\omega}^T\varphi(\mathbf{x}_i) + \mathbf{b} + \mathbf{e}_i - \mathbf{y}_i = 0 \end{cases} \tag{17}$$

Put Equation (17) into the regression function (13) to obtain an analytical solution to the optimization problem:

$$\begin{bmatrix} 0 & \mathbf{I}_N^T \\ \mathbf{I}_N & \boldsymbol{\Omega} + c^{-1}\mathbf{I} \end{bmatrix} \begin{bmatrix} \mathbf{b} \\ \alpha \end{bmatrix} = \begin{bmatrix} 0 \\ \mathbf{y} \end{bmatrix} \tag{18}$$

where $\mathbf{y} = [y_1, \ldots, y_n]^{\mathrm{T}}$, $\mathbf{I}_{\mathrm{N}} \in \mathbf{R}^{\mathrm{N}}$, $\boldsymbol{\Omega} = k(\mathbf{x}_i, \mathbf{x}_j)$ is the Gaussian kernel satisfying the Mercer condition.

The regression equation for the inverse system is:

$$\mathbf{y}(\mathbf{x}) = \sum_{i=1}^{n}\alpha_i k(\mathbf{x}, \mathbf{x}_i) + \mathbf{b} \tag{19}$$

where $K(\mathbf{x}, \mathbf{x}_i) = \exp(\frac{-||\mathbf{x}-\mathbf{x}_i||^2}{2\sigma^2})$ is the Gaussian kernel function, and σ^2 is the kernel width.

3.2. GWO Algorithm

GWO is an intelligent group optimization algorithm that simulates the hierarchical level and hunting mechanism of natural grey wolves. It is widely used for the advantages of fewer parameters, easy implement, strong convergence and so on in the field of parameter optimization.

The hierarchy of the pyramid of the grey wolves group is shown in Fig. 3. The figure shows that the top leader γ wolves are at the top of the pyramid and are responsible for feeding and making decisions. In the second level of the pyramid, ε wolves are mainly responsible for making decisions and feed the information back to other wolves. The η wolves are located in the third layer of the pyramid and are the executor of γ wolves and ε wolves decisions. At the bottom of the pyramid is θ wolves, who are responsible for helping to catch prey.

In the GWO, γ wolves lead other wolves to find and capture the prey. When the grey wolves are very small from the prey range, γ wolves command b wolves and η wolves to siege the prey and let θ wolves kill the prey. The position update process of the individual grey wolf is shown in Fig. 4.

The implementation of the GWO includes three main parts:

(1) surrounding the prey

The behavior of wolves encircling their prey can be expressed as:

$$\begin{cases} \vec{D} = \left|\vec{V} \cdot \vec{X}_p(t) - \vec{X}(t)\right| \\ \vec{X}(t+1) = \vec{X}_p(t) - \vec{A} \cdot \vec{D} \\ \vec{A} = \vec{z}\left(2\vec{h}_1 - 1\right) \\ \vec{V} = 2\vec{h}_2 \end{cases} \tag{20}$$

where $\vec{D}$ is the distance to the prey; t is the number of updates; $\vec{V}$ and $\vec{A}$ are the coefficient vector; $\vec{X}(t)$ is the position vector of the grey wolf after t iteration; $\vec{X}(t+1)$ is the position vector of the grey wolf after $t+1$ iteration; $\vec{X}_p(t)$ is the position vector of the prey after t iteration; $\vec{h}_1$, $\vec{h}_2$ are random values within [0, 1]; $\vec{z}$ is the convergence factor; and the value range is [0, 2].

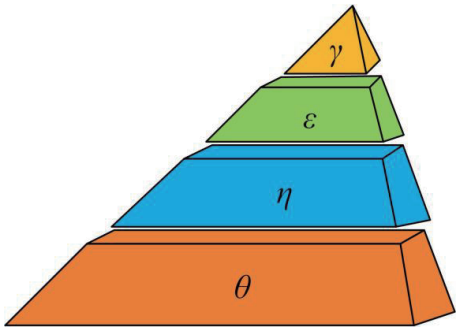

FIGURE 3. Wolf pack level pyramid structure diagram.

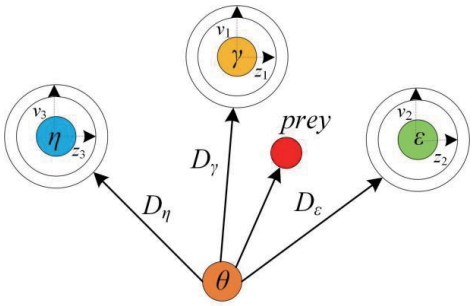

FIGURE 4. Grey wolf location update process diagram.

(2) Eating prey on prey

When the grey wolf is hunting, the three wolves γ, ε, and η seek and approach the prey. The mathematical expression of this process is as follows:

$$\begin{cases} \vec{D}_\gamma = \left|\vec{V}_1 \cdot \vec{X}_\gamma - \vec{X}\right| \\ \vec{D}_\varepsilon = \left|\vec{V}_2 \cdot \vec{X}_\varepsilon - \vec{X}\right| \\ \vec{D}_\eta = \left|\vec{V}_3 \cdot \vec{X}_\eta - \vec{X}\right| \end{cases} \tag{21}$$

where $\vec{X}_\gamma$, $\vec{X}_\varepsilon$, and $\vec{X}_\eta$ represent the optimal positions of γ, ε, η, respectively; $\vec{D}_\gamma$, $\vec{D}_\varepsilon$, $\vec{D}_\eta$ represent the distance between the γ, ε and η optimal wolf and prey, respectively; $\vec{V}_1$, $\vec{V}_2$, $\vec{V}_3$ are the corresponding random coefficient vectors; $\vec{X}$ represents the position vector of the grey wolf.

To update the location of the grey wolf population through the leadership of γ, ε, and η:

$$\begin{cases} \vec{X}_1 = \left|\vec{X}_\gamma - \vec{A}_1\vec{D}_\gamma\right| \\ \vec{X}_2 = \left|\vec{X}_\varepsilon - \vec{A}_2\vec{D}_\varepsilon\right| \\ \vec{X}_3 = \left|\vec{X}_\eta - \vec{A}_3\vec{D}_\eta\right| \end{cases} \tag{22}$$

$$\vec{X}(t+1) = \frac{\left(\vec{X}_1 + \vec{X}_2 + \vec{X}_3\right)}{3} \tag{23}$$

where $\vec{A}_1$, $\vec{A}_2$, $\vec{A}_3$ are the calculated different coefficients; $\vec{X}_1$, $\vec{X}_2$, $\vec{X}_3$ represent the updated positions of γ, ε, and η, respectively.

(3) Attacking the prey

Attacking the prey to determine the position of the prey is also the process of obtaining the optimal solution, which is mainly realized by decreasing the convergence factor $\vec{z}$ from 2 to 0 in the iterative process, and the group obtains the optimal solution after the iteration. Since the value of $\vec{z}$ is decreased, $\vec{A}$ is also decreased in $[-2z, 2z]$. When $\left|\vec{A}\right| \leq 1$, the wolves are forced to attack the prey. When $\left|\vec{A}\right| > 1$, the grey wolves are forced to diverge from the prey.

3.3. Improvements of the GWO

(1) Nonlinear adjustment of the convergence factor

The efficient global search function ensures that the algorithm is not localized optimal solution, and efficient local search function ensures more accurate data and better algorithm convergence. The size of the convergence factor directly affects the optimization performance of the algorithm. At $\left|\vec{A}\right| \leq 1$, the local search capability is strengthened, and the convergence rate increases; at $\left|\vec{A}\right| > 1$, the global search capability is high. In the traditional GWO, the convergence factor z decreases linearly with the increase of iterations, which is not consistent with the actual optimization process, and there are problems such as falling into local optimum and slow convergence rate. Therefore, the convergence factor is adjusted nonlinearly, and the adjustment formula is:

$$z = (z_{\max} - z_{\min})\left(1 - \sin\left(\frac{\pi t}{2T_{\max}}\right)^\lambda\right) \tag{24}$$

where $z_{\max}$ is equal to 2, which is the maximum of z, and $z_{\min}$ is equal to 0, which is the minimum of z. λ is the adjustment parameters which is equal to 3 in this paper; t is the current iterations, and $T_{\max}$ is the maximum number of iterations. The comparison of the convergence before and after the improvement is shown in Fig. 5.

As can be seen from Fig. 5, in the early iteration stage, the reduced rate of the improved z is slower, which is beneficial for jumping out of the local optimal and improving the global search efficiency. In the late iteration stage, the reduced rate of the improved z is rapid, which is beneficial for the algorithm convergence and improvement of the accuracy of local search. It follows that the improved convergence factor balances the overall search power of the algorithm.

(2) Adaptive location update strategy

During the iteration of the GWO, without reaching the original γ, ε, and η solutions, the pack still updates to this position. At this time, the wolves cannot find the global optimum and the global optimal solution. Therefore, in order to avoid hunting failure due to superior wolves judgment errors, this paper proposes an adaptive position updating strategy. In traditional

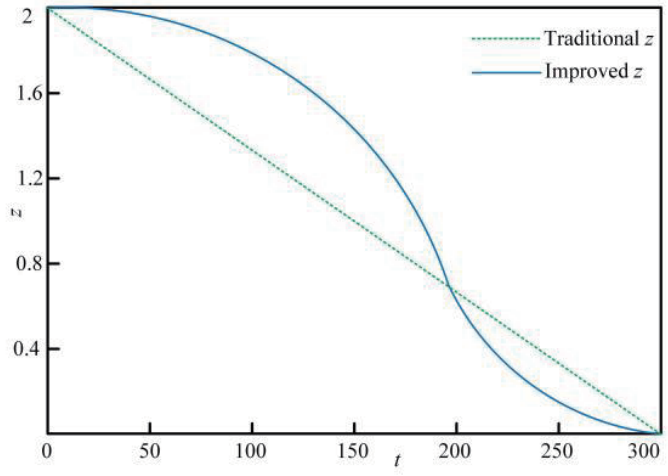

FIGURE 5. Comparison of the convergence before and after the improvement.

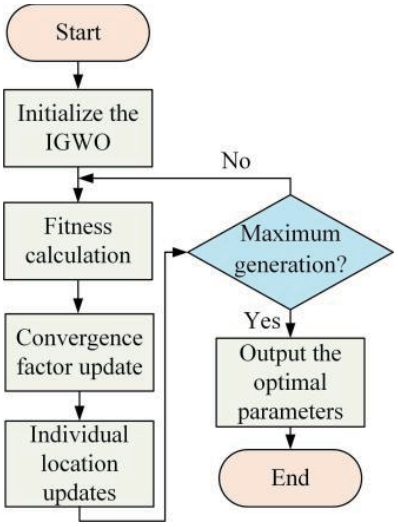

FIGURE 6. Flow chart of the optimization parameters of the IGWO.

GWO, the grey wolf individual position update does not consider γ, ε, η three wolves between class and decision-making ability, and this paper according to the proportion of fitness value calculation three wolves weight γ, ε, η makes each individual quickly move to the optimal position, grey wolves individual to γ, ε, η three wolves distance weight expression are:

$$\begin{cases} W_1 = \dfrac{|\vec{X}_1|}{|\vec{X}_1|+|\vec{X}_2|+|\vec{X}_3|+k} \\ W_2 = \dfrac{|\vec{X}_2|}{|\vec{X}_1|+|\vec{X}_2|+|\vec{X}_3|+k} \\ W_3 = \dfrac{|\vec{X}_3|}{|\vec{X}_1|+|\vec{X}_2|+|\vec{X}_3|+k} \end{cases} \tag{25}$$

where to avoid a zero denominator, k takes the constant 10^{-9}.

At the same time, according to the weight formula, the adaptive formula for the individual position update of grey wolves is proposed as

$$\vec{X}(t+1) = \frac{W_1\vec{X}_1 + W_2\vec{X}_2 + W_3\vec{X}_3}{3}\left(1 - \frac{t}{T_{\max}}\right) + \vec{X}_1\frac{t}{T_{\max}} \tag{26}$$

4. THE ESTABLISHMENT OF IGWO-LSSVM GENERALIZED INVERSE SYSTEM

4.1. Parameter Optimization Based on IGWO

The kernel function parameter and regularization parameter affect the decoupling performance of the LSSVM inverse system, so IGWO is selected for its optimal configuration. The flow of the IGWO for finding the parameters of the kernel function and the regularization parameters is shown in Fig. 6.

1) The GWO is initialized, and the relevant parameters include the dimension of the input data set, the optimization boundary, the number of iterations, and the location of the initial wolf pack.

2) Initialize the wolf population and use σ and c to describe the location vector for each wolf.

3) Update the convergence factor and the individual location of the grey wolf according to Equations (23), (24), and (25), respectively.

4) Determine whether the number of iterations has reached the maximum, and if so, end the iteration and get the optimized parameters. Otherwise, skip to step 3 to optimize the parameters continuously.

5) Output the optimal parameters σ and c.

In order to verify the superiority of IGWO, the parameters of LSSVM are optimized by using different methods respectively. Fig. 7 shows the comparison curves of iterative convergence, where the yellow line is PSO; the blue line is GA; the red line is IGWO. As can be seen from Fig. 6, the curve of IGWO is smoother than others. The number of iterations using PSO is 92, and the fitness value tends to be stable. The number of iterations using GA is 58, and the fitness value tends to be stable. The number of iterations using IGWO is 41, and the fitness value tends to be stable. From the comparison results, it can be found that the IGWO has higher convergence accuracy and not easy to fall into the local optima.

4.2. Decoupling Modeling Based on IGWO-LSSVM Inverse System

In general, in order to better decouple the multi-input and multi-output the BPMSM system into a simple system, the right inverse system function is Equation (12), selecting $a_{10} = 1$, $a_{11} = 1.414$, $a_{12} = 1$, $a_{20} = 1$, $a_{21} = 1.414$, $a_{22} = 1$, $a_{30} = 1$, $a_{31} = 1$. BPMSM is eventually decoupled into the simplest one first-order and two second-order systems, as shown in Fig. 8.

To verify the fitting effects of the IGWO-LSSVM, the rotor displacement is used as an example to test the output characteristics of fitting based on the LSSVM inverse system and

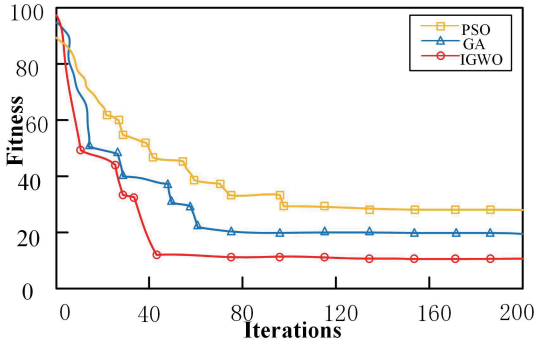

FIGURE 7. Comparison curves of iterative convergence.

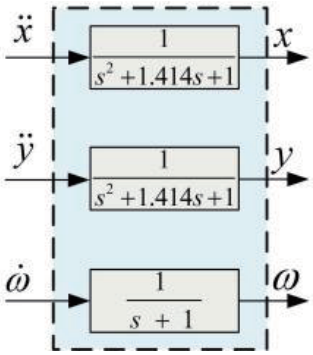

FIGURE 8. Equivalent pseudo-linear system.

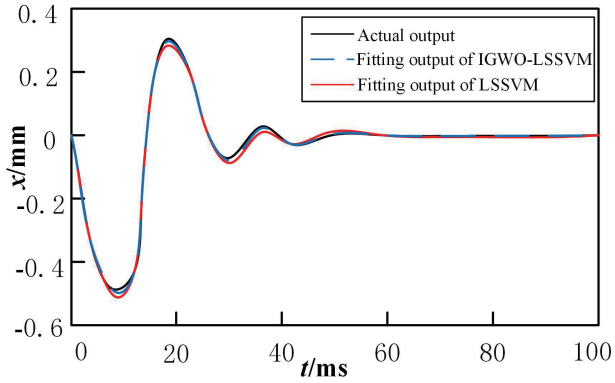

FIGURE 9. The fitting performance cures.

IGWO-LSSVM inverse system. Fig. 9 shows the fitting performance cures, where the black line is the actual output radial displacement of the system model simulation; the dotted line is the IGWO-LSSVM inverse system tracking output of the motor; and the red line is the LSSVM inverse system tracking output of the motor. As can be seen from Fig. 9, the IGWO-LSSVM inverse system can well realize the displacement fitting output to the system, and the fitting accuracy is higher than the LSSVM.

The specific steps for identifying the generalized inverse system of the BPMSM are as follows:

(1) Acquisition of the data samples. The simulation model is excited by inputting the random current excitation signal, setting the sampling time of 0.1 ms and the running time of 1 s to sample the motor speed and radial displacement output signal. 1000 sets of sample data are obtained. The input variable is $\mathbf{X} = (\ddot{\mathbf{x}}, \dot{\mathbf{x}}, \mathbf{x}, \dot{\mathbf{y}}, \dot{\mathbf{y}}, \mathbf{y}, \dot{\boldsymbol{\omega}}, \boldsymbol{\omega})^T$, and the output variable is $\mathbf{Y} = (\mathbf{i}_{md}, \mathbf{i}_{mq}, \mathbf{i}_{bd}, \mathbf{i}_{bq})^T$, 70% as the training sample and 30% as the test sample.

(2) Training of the LSSVM. Based on the LSSVM input obtained from sampling, sample data are output, training on LSSVM and establishing inverse model of the BPMSM, and using the IGWO algorithm to optimize the σ and c. The improved parameters enable the output value of LSSVM to better approximate the expected value.

(3) Fig. 10 is the decoupling control block diagram of the BPMSM, which is mainly composed of an inverse system of the original system obtained by IGWO-LSSVM and the compound controlled object. The proportional integral differential (PID) and proportional integral (PI) modules are used for system displacement and rotational speed regulation, respectively.

5. SIMULATION TEST

In order to verify the feasibility and superiority of the method proposed in this paper, conduct simulation tests and compare with the traditional LSSVM inverse system control method under the same conditions, and the specific simulation results are analyzed as follows. The parameters of BPMSM used in the simulation are shown in Table 1.

The simulation curves of the dynamic decoupling of the BPMSM are shown in Fig. 11. From 0 s to 0.25 s, the speed is 3000 r/min, and after 0.25 s, adjust the given speed to 5000 r/min. As can be seen from Fig. 11, under the traditional LSSVM inverse system control method, it takes 65 ms to reach the maximum, and it is adjusted by 26 ms to reach the steady state. The overshoot is 6%. Under the proposed method, it takes 57 ms to reach the maximum, reaching the steady state of 14 ms, and the overshoot is 2%. At the same time, under the traditional LSSVM inverse system control method, the disturbance amplitudes of the radial displacement in the x- and y-directions are 22 μm and 28 μm, respectively, while the radial displacement in the x- and y-directions has basically

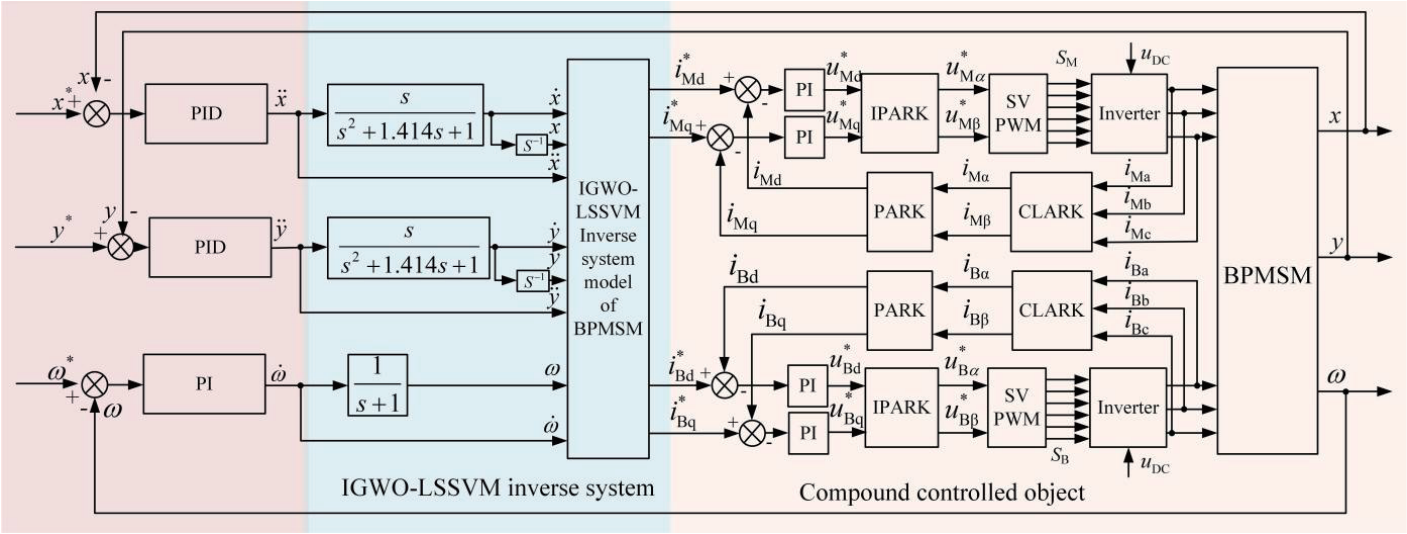

FIGURE 10. Block diagram of decoupling control of BPMSM based on IGWO-LSSVM inverse system.

TABLE 1. Parameters of the prototype machine.

Symbol	Quantity	Value
U_n	Rated voltage (V)	220
P_n	Rated power (kW)	1.1
n_n	Rated speed (r/min)	5000
P_M	Pole-pair number of torque windings	2
P_B	Pole-pair number of suspension force windings	1
δ	Air gap length (mm)	2
δ_0	Air gap length of the auxiliary bearing (mm)	0.3
Ψ_f	Flux of the permanent magnet (Wb)	0.125
m	Rotor mass (kg)	0.8

no disturbance under the method proposed in this paper. The simulation tests prove that the proposed method has a better speed adjustment performance and dynamic decoupling performance.

The simulation curves of the static decoupling of the BPMSM are shown in Fig. 12. After a stable suspension of the rotor, at $t = 0.2$ s, a 100 μm step signal is given to the x direction. Under the traditional LSSVM inverse system control method, the overshoot of the displacement curve in the x direction is 48%, and the adjustment time is 44 ms. Due to the coupling relationship between the suspended force currents, a disturbance with the amplitude of 33 μm is caused in the y direction. Under the control method, the displacement curve in the x direction underwent an adjustment time of 20 ms to reach 100 μm almost without overshoot, and the displacement curve in the y direction is generated without a disturbance. The simulation tests show that the proposed method can achieve decoupling control between x direction displacement and y direction displacement with excellent performance.

The comparative curves of anti-interference performance simulation tests of the BPMSM are shown in Fig. 13. When the rotor is running at 5000 r/min and stably suspended, a 20 N interference force is applied to the rotor at $t = 0.15$ s and $t = 0.35$ s along the x- and y-directions, respectively. Under the traditional LSSVM inverse system control method, the disturbance amplitudes of the radial displacement in the x- and y-directions are 32 μm and 36 μm, respectively, and the adjustment time is 50 ms, while under the proposed control method, the disturbance amplitudes in the x- and y-directions are 24 μm and 30 μm, respectively, and the adjustment time is about 38 ms. The simulation proves that the proposed method has superior anti-interference performance and better robustness.

6. EXPERIMENT RESEARCH

6.1. Experimental Platform and Prototype Parameters

In order to verify the feasibility of the IGWO-LSSVM inverse system decoupling control method, the experimental plat-

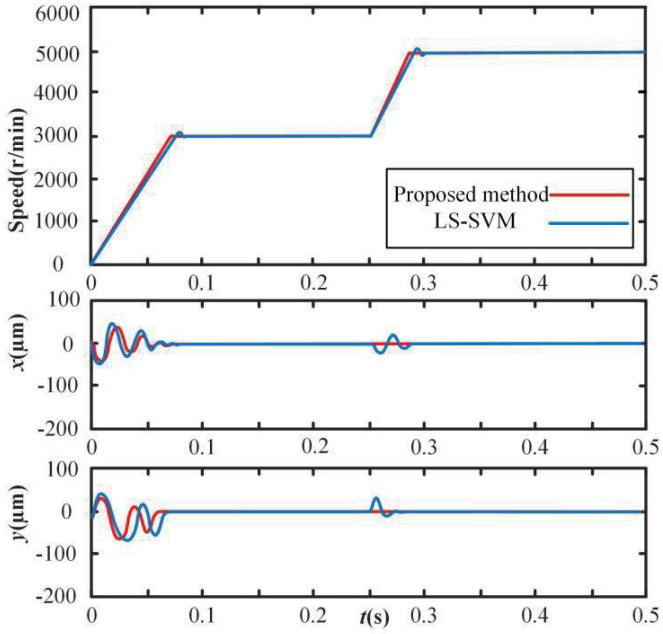

FIGURE 11. Simulation curves of dynamic decoupling of the BPMSM.

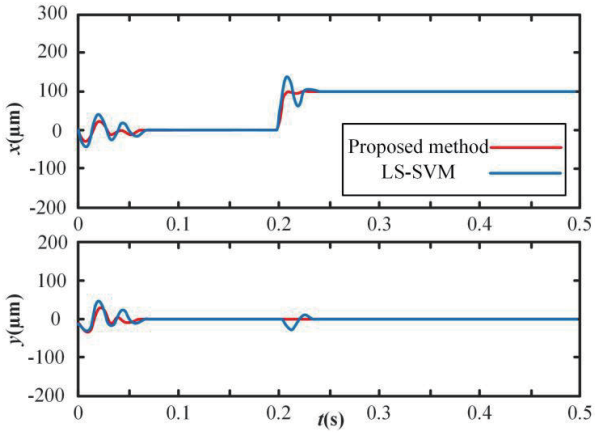

FIGURE 12. Simulation curves of static decoupling of the BPMSM.

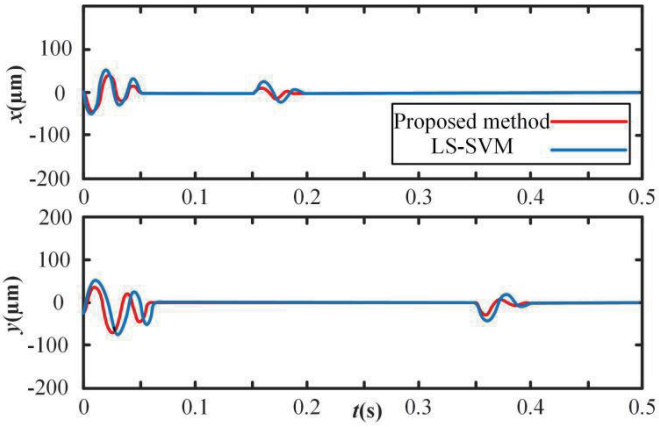

FIGURE 13. Displacement simulation curves of anti-interference of the BPMSM.

form with DSP TMS320F28335 as the core digital controller as shown in Fig. 14 is constructed, mainly including: the BPMSM prototype, digital signal processor (DSP), eddy current sensor, DC power, and power drive circuit board. The relevant parameters of the experimental prototype are shown in Table 1. The specific control process of the BPMSM is as follows. As shown in Fig. 14, the master computer uses the simulator to write the program into the DSP. After the rotor positioning, the BPMSM pulse signal and check signal are obtained by the photoelectric encoder, which are input into the DSP through the signal conditioning circuit to obtain the speed of rotation and the direction of rotation at this time. The x- and y-axis displacement signal of the rotor is obtained by using the eddy current sensor and input into the DSP. According to the speed and displacement signal, DSP outputs two sets of pulse width modulation (PWM) waves to the power drive circuit board and generates the three-phase suspension force windings control current and the three-phase torque windings control current, so as to realize the real-time control.

6.2. Dynamic Decoupling Experiment

The experimental waveforms of rotational speed and radial displacement in the x- and y-directions when the speed accelerates from 3000 r/min to 5000 r/min are shown in Fig. 15.

As shown in Fig. 15, when the speed of the motor accelerates from 3000 r/min to 5000 r/min, the overshoot of the traditional LSSVM inverse system control method is 8%, and the regulation time is 161 ms, while the regulation time is 82 ms of the proposed method, and there is almost no overshoot. For the radial displacement, the disturbance amplitudes of the traditional LSSVM inverse system control method are 39 μm and 48 μm

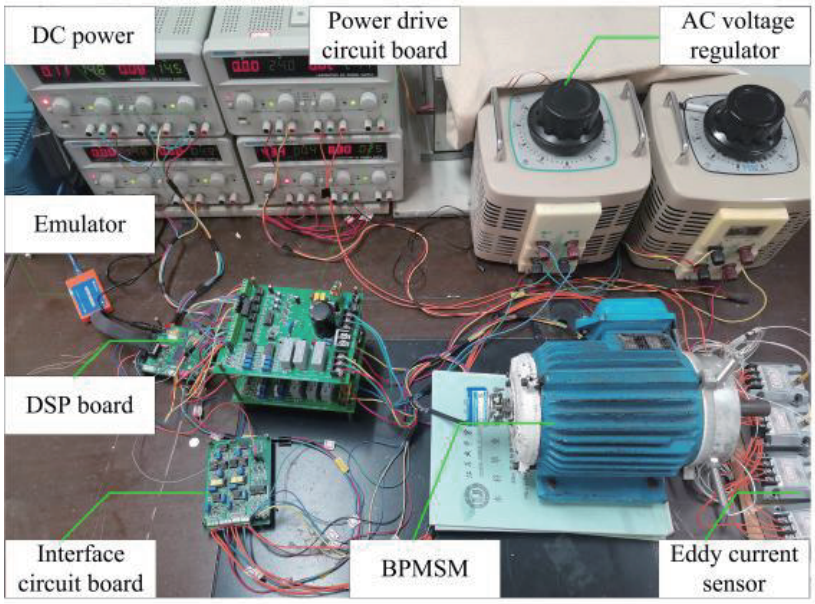

FIGURE 14. The BPMSM experimental platform.

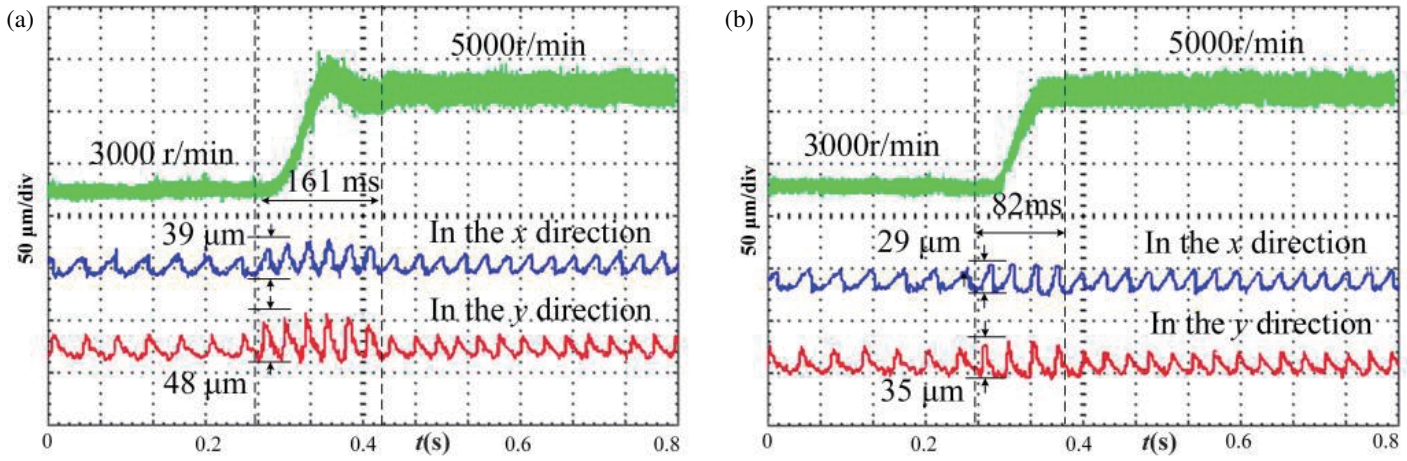

FIGURE 15. Experimental waveforms of dynamic decoupling performance under different methods. (a) Traditional LSSVM inverse system control. (b) Proposed method.

in the x- and y-directions, respectively, while the disturbance amplitudes in the x- and y-directions of the proposed method are reduced by 25.6% and 27.1%, respectively. The experimental waveforms of dynamic decoupling show that the proposed method has better speed regulation performance and superior dynamic decoupling performance.

6.3. Static Decoupling Experiment

Figure 16 is the experimental waveforms of the static decoupling performance of the BPMSM control system, giving a paranoid signal of 100 μm along the x direction when the motor is suspended stably. The overshoot of the traditional LSSVM inverse system control method is 31% in the x direction, and the adjustment time is 93 ms, while the overshoot of the method proposed in this paper is 5% in the x direction, and the adjustment time is 67 ms. Because the suspension force control current is coupled in the x- and y-directions, after applying the bias signal, the displacement waveforms in the y direction produce a peak disturbance of 28 μm under the traditional inverse system control method, while under the proposed control method, the displacement waveforms in the y direction is generated without disturbance. The experimental results prove that the proposed IGWO-LSSVM inverse system decoupling control method has superior static decoupling performance and can better realize the decoupling control between suspension forces.

6.4. Disturbance Experiment

The anti-interference experimental waveforms of the system under different control methods are shown in Fig. 17. When the motor is running at 5000 r/min and stably suspended, a 20 N

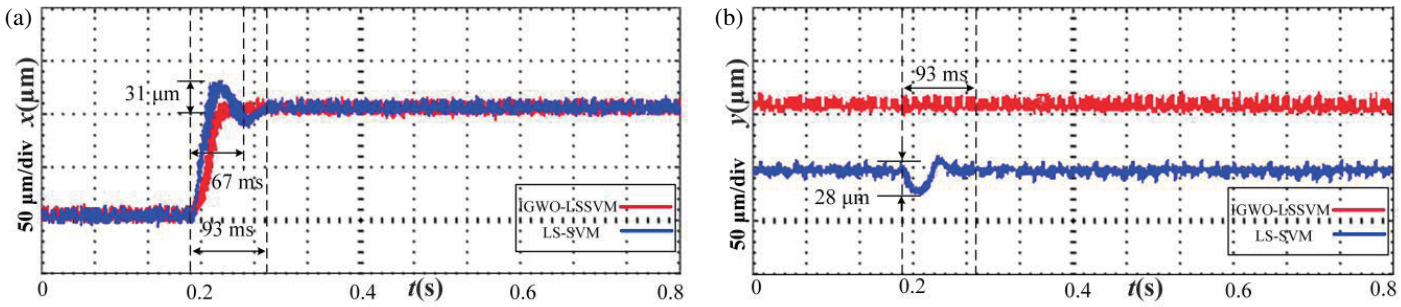

FIGURE 16. Experimental waveforms of static decoupling performance (a) displacement waveforms in the x direction (b) displacement waveforms in the y direction.

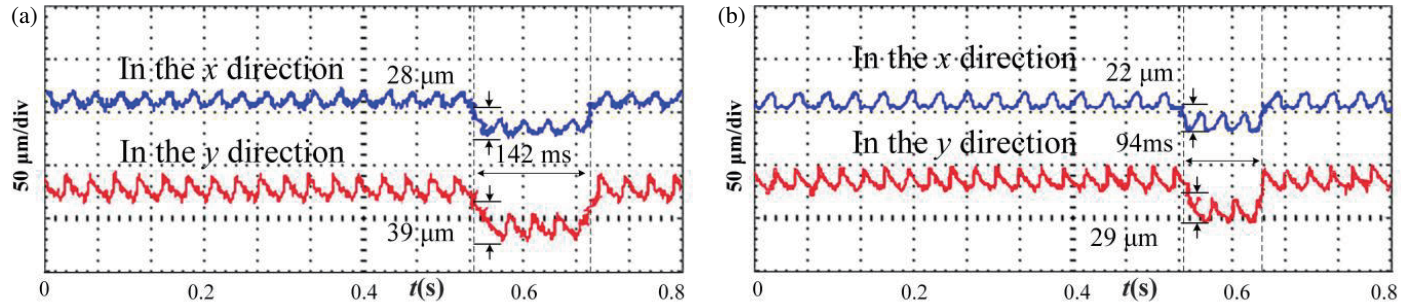

FIGURE 17. Anti-interference experimental waveforms of BPMSM. (a) Traditional LSSVM inverse system control. (b) Proposed method.

force is applied to the rotor along the y direction. Because of the coupling relationship of the suspension force control current in the x- and y-directions, the continuous interference force causes the fluctuation in the x- and y-directions. It is known from Fig. 17(a), based on the traditional LSSVM inverse system control method, the disturbance amplitudes are 28 μm and 39 μm in the x- and y-directions, respectively, and the adjustment time is 142 ms. It is known from Fig. 17(b) that based on the decoupling control method proposed in this paper, the disturbance amplitudes are 22 μm and 29 μm in the x- and y-directions, respectively, and the adjustment time is 94 ms. The disturbance amplitude is reduced by 21.4% and 25.6% in the x- and y-directions, respectively, and the adjustment time is reduced by 33.8% under the proposed method in this paper. The experimental results prove that the proposed decoupling control method has superior decoupling performance and anti-interference ability.

7. CONCLUSION

The characteristics of nonlinear and strong coupling of the BPMSM hinder its development to the field of high speed and high precision. To achieve the dynamic decoupling of the BPMSM torque and radial suspension force, a kind of decoupling control method for the inverse system based on IGWO-LSSVM is proposed in this paper. The following conclusions are obtained:

1) The mathematical model of the BPMSM is established, and its reversibility is proved, while optimizing the kernel function parameters and regularization parameters of LSSVM through IGWO to fit the inverse system more precisely.

2) The decoupling performance of the BPMSM under the proposed IGWO-LSSVM inverse system control method and the traditional LSSVM inverse system control method are compared, and the feasibility and superiority of the proposed method are proved.

3) The BPMSM digital control system is constructed, and the rotational speed response experiments and anti-interference experiments are performed, which further verifies that the proposed method has superior dynamic and static decoupling performance and anti-interference characteristics.

ACKNOWLEDGEMENT

This project was sponsored in part by National Natural Science Foundational of China (62273168).

REFERENCES

[1] Bosch, R., "Development of a bearingless electric motor," in *Proceedings of International Conference of Electric Machines*, 373–375, Pisa, Italy, 1988.

[2] Peralta, P., T. Wellerdieck, D. Steinert, T. Nussbaumer, and J. W. Kolar, "Ultra-high temperature (250°C) bearingless permanent magnet pump for aggressive fluids," *IEEE/ASME Transactions on Mechatronics*, Vol. 22, No. 5, 2392–2394, Oct. 2017.

[3] Sun, X., L. Chen, and Z. Yang, "Overview of bearingless permanent-magnet synchronous motors," *IEEE Transactions on Industrial Electronics*, Vol. 60, No. 12, 5528–5538, Dec. 2013.

[4] Xu, Y. and H. Zhu, "Overview of the development of bearingless permanent magnet synchronous motor system and its key technologies," *Proceeding of the CSEE*, Vol. 39, No. 10, 2994–3007, May 2019.

[5] Morawiec, M., "The adaptive backstepping control of permanent magnet synchronous motor supplied by current source inverter," *IEEE Transactions on Industrial Informatics*, Vol. 9, No. 2, 1047–1055, May 2013.

[6] Asama, J., T. Asami, T. Imakawa, A. Chiba, A. Nakajima, and M. A. Rahman, "Effects of permanent-magnet passive magnetic bearing on a two-axis actively regulated low-speed bearingless motor," *IEEE Transactions on Energy Conversion*, Vol. 26, No. 1, 46–54, Mar. 2011.

[7] Sun, Y., D. Fei, and H. Zhu, "Study on decoupling control of the 5 degree-of-freedom bearingless permanent magnet motor based on α-th order inverse system method," *Proceedings of the CSEE*, Vol. 26, No. 1, 120–127, Jan. 2006.

[8] Li, Q. and X. Liu, "Decoupling control of bearingless induction motor based on rotor flux orientation with inverse system theory," in *2010 International Conference on Measuring Technology and Mechatronics Automation*, 894–897, Changsha, China, Mar. 2010.

[9] Zhu, H. and Z. Gu, "Active disturbance rejection control of 5-degree-of-freedom bearingless permanent magnet synchronous motor based on fuzzy neural network inverse system," *ISA Transactions*, Vol. 101, 295–308, Jun. 2020.

[10] Zhu, H. and W. Du, "Decoupling control of bearingless permanent magnet synchronous motor based on fuzzy neural network inverse system," *Proceedings of the CSEE*, Vol. 39, No. 4, 1190–1198, Feb. 2019.

[11] Xu, B., H. Zhu, and X. Wang, "Decoupling control of outer rotor coreless bearingless permanent magnet synchronous motor based on least squares support vector machine generalized inverse optimized by improved genetic algorithm," *IEEE Transactions on Industrial Electronics*, Vol. 69, No. 12, 12 182–12 190, Dec. 2022.

[12] Zhang, J., M. M. Lin, F. Shi, *et al.*, "Setpoint optimization of organic langken cycle control system," *Chinese Science Bulletin*, Vol. 59, No. 11, 2792–2798, Sep. 2014.

[13] Bu, W. and Z. Li, "LS-SVM inverse system decoupling control strategy of a bearingless induction motor considering stator current dynamics," *IEEE Access*, Vol. 7, 132 130–132 139, Sep. 2019.

[14] Sun, Y., Y. Liu, and H. Liu, "Temperature compensation for a six-axis force/torque sensor based on the particle swarm optimization least square support vector machine for space manipulator," *IEEE Sensors Journal*, Vol. 16, No. 3, 798–805, Feb. 2016.

[15] Mirjalili, S., S. M. Mirjalili, and A. Lewis, "Grey wolf optimizer," *Advances in Engineering Software*, Vol. 69, 46–61, Mar. 2014.

[16] Xu, L., H. Wang, W. Lin, T. A. Gulliver, and K. N. Le, "GWO-BP neural network based OP performance prediction for mobile multiuser communication networks," *IEEE Access*, Vol. 7, 152 690–152 700, Oct. 2019.

[17] Liao, W., L. Zhou, C. Zhang, D. Wang, J. Zhang, and L. Guo, "A method for discriminating the moisture status of OIP bushing based on Dissado-hill and GWO-HMM model," *IEEE Transactions on Industry Applications*, Vol. 58, No. 2, 1512–1520, Mar.-Apr. 2022.

[18] Li, K., G. Cheng, X. Sun, and Z. Yang, "A nonlinear flux linkage model for bearingless induction motor based on GWO-LSSVM," *IEEE Access*, Vol. 7, 36 558–36 567, 2019.

[19] Zhu, H. and H. Li, "Magnetic field equivalent current analysis-based radial force control for bearingless permanent magnet synchronous motors," *Energies*, Vol. 8, No. 6, 4920–4942, May 2015.

[20] Zhao, H., G. Huang, and N. Yan, "Forecasting energy-related CO_2 emissions employing a novel SSA-LSSVM model considering structural factors in China," *Energies*, Vol. 11, No. 4, 781, Mar. 2018.